RESEARCH ARTICLE
PLANETARY SCIENCES

Earth and Planetary Physics
7: 229–236, 2023
doi: 10.26464/epp2023030

Are cyclones in Jupiter's polar regions modulated by the radially directional Rayleigh–Taylor instability?

ChuXin Chen*

Chinese Academy of Sciences Key Laboratory of Geospace Environment, Department of Geophysics and Planetary Sciences, School of Earth and Space Sciences, University of Science and Technology of China, Hefei 230026, China

Key Points:

- Cyclones in Jupiter's polar regions are modulated by the radially directional Rayleigh–Taylor instability.
- The Rayleigh–Taylor instability is driven by centrifugal force and the negative temperature gradient with respect to latitude.
- The temperature gradient is due to solar radiation resulting from the small axial inclination of Jupiter.

Citation: Chen, C. X. (2023). Are cyclones in Jupiter's polar regions modulated by the radially directional Rayleigh–Taylor instability?. *Earth Planet. Phys.*, *7*(2), 229–236. http://doi.org/10.26464/epp2023030

Abstract: The persistence and symmetry of cyclones around the poles of Jupiter are unknown. In the present investigation, inspired by cyclones at the South Pole of the Earth, we propose a mechanism that provides an explanation for this problem. The negative temperature gradient with respect to latitude may play an important role here. This temperature gradient is induced by solar radiation because of the small axial inclination of Jupiter. Our numerical simulations suggest that cyclones in the polar regions of Jupiter may be modulated or controlled by the radially directional Rayleigh–Taylor instability, driven by centrifugal force and the negative temperature gradient along the latitude.

Keywords: cyclone; polar region of Jupiter; temperature gradient along the latitude; Rayleigh–Taylor instability

1. Introduction

The Juno probe (Bolton et al., 2017; Connerney et al., 2017), equipped with infrared (Jovian Infrared Auroral Mapper, or JIRAM; Adriani et al., 2017) and visible (JunoCam; Hansen et al., 2014) cameras, revealed unprecedented views of Jupiter's polar regions (Adriani et al., 2018). Eight cyclones appear around the north polar cyclone, and five cyclones appear around the south polar cyclone. These cyclones have preserved their individual morphologies over several months. Saturn, the sister planet of Jupiter, on the other hand, has only a single cyclone at each of its poles. What causes the difference in the polar region cyclones between these two planets has recently attracted considerable attention.

Because of the turbulent characteristics of flow, cyclones at higher latitudes are expected from the transition of axisymmetric zones and belts as the latitude increases. The β effect (Rhines, 1975) would predict the motion of cyclones toward the poles (Shapiro, 1992; O'Neill et al., 2015) and the merger of cyclones, as on Saturn.

Several authors have carried out investigations of vortices. Theiss (2006) studied the formation of a vortex caused by suppression of a generalized Rhines effect at the polar region. Afanasyev and Huang YC (2020) simulated the polarward translation of vortices. Reinaud and Dritschel (2019) investigated the stability and nonlinear evolution of vortices.

For cyclones in Jupiter's polar region, the reasons for their persistence, close clustering, and symmetry around each of the poles are still not clear. It is noteworthy that cyclones also cluster around the South Pole of the Earth, where the Antarctic continent is fully surrounded by ocean. Thus, there may be some similarity between the cyclones of Jupiter and those of the Earth.

The symmetry of cyclones around the poles reminds us that some quantity or boundary of domain must exist that is symmetric around the poles. Inspired by cyclones around the South Pole of the Earth, we speculate that this quantity is the negative gradient of temperature along the latitude. This negative temperature gradient is due to solar radiation, a heat source that has been ignored in previous studies.

Some basic conditions may exist in the Jovian polar regions that contribute to the development of a centrifugal force-driven Rayleigh–Taylor instability. First, Jupiter spins at a period of 10 hours, and the centrifugal force points radially outward. Second, the spin axis is nearly perpendicular to the ecliptic surface. The component of solar radiation perpendicular to the surface of Jupiter is a cosine function of latitude. The resulting temperature gradient is a negative sine function of latitude. The maximum temperature gradient is in the polar regions, where the sine function reaches one as the latitude approaches 90°.

In this article, we numerically investigate the formation of

Correspondence to: C. X. Chen, chuxin@ustc.edu.cn
Received 20 OCT 2022; Accepted 30 DEC 2022.
Accepted article online 13 FEB 2023.

cyclones in the polar regions of Jupiter. The mathematical formulation is described in Section 2. The results are provided in Section 3, and finally, a discussion and the conclusions are presented in Section 4.

2. Mathematical Formulation

To emphasize the key factors that may modulate or control the pattern of cyclones, we simplify the geometry to a two-dimensional problem (Zhang KK et al., 1999; Chen CX and Zhang KK, 2002). The plane under consideration is perpendicular to the angular velocity of Jupiter (Figures 1 and 2). For the symmetry of the problem, we focus on an annulus with an inner boundary at r_i and an outer boundary at r_o.

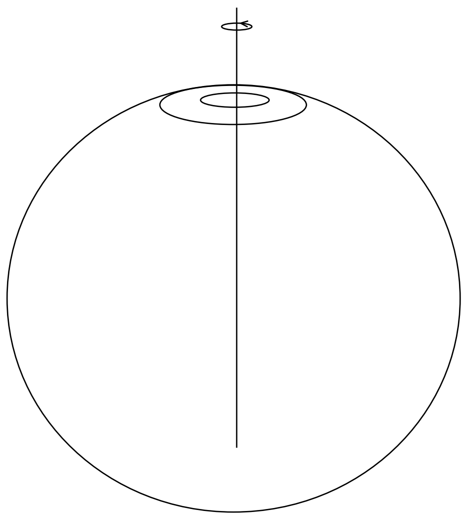

Figure 1. Schematic diagram showing the calculated domain on Jupiter. The large circle represents Jupiter. The vertical straight line through the center of the large circle represents the spin axis of Jupiter. The region between the two concentric circles around the spin axis is the calculated domain. The circle with an arrow represents the spin direction of Jupiter.

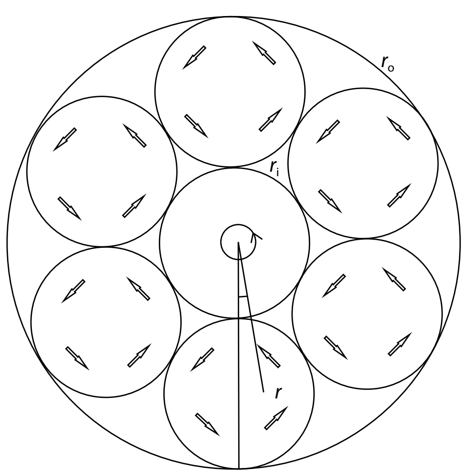

Figure 2. Schematic diagram showing the calculated domain on Jupiter from a bird's-eye view above the polar region. The two concentric circles without arrows represent the calculated domain. The circles with four arrows represent the cyclones. The circle with an arrow represents the spin direction of Jupiter. The polar coordinate system is used.

By defining η, the ratio of the radius of the inner boundary to the outer boundary, as

$$\eta = \frac{r_i}{r_o},$$

the inner boundary and the outer boundary can be expressed as

$$r_i = \frac{\eta}{1-\eta}, \quad r_o = \frac{1}{1-\eta},$$

where r_i and r_o are now dimensionless.

The momentum equation is

$$\rho\frac{d\boldsymbol{u}}{dt} = -\nabla p + \mu\nabla^2\boldsymbol{u} + 2\rho\boldsymbol{u}\times\boldsymbol{\Omega} + \rho\Omega^2\boldsymbol{r}, \quad (1)$$

where ρ is density, $\boldsymbol{u}$ is velocity, p is pressure, μ is dynamic viscosity, $\boldsymbol{\Omega}$ is the angular velocity of Jupiter, and $\boldsymbol{r}$ is the distance from the axis of rotation of Jupiter.

The heat transfer equation is

$$\frac{DT}{Dt} = \kappa\nabla^2 T, \quad (2)$$

where T is temperature, κ is thermal diffusivity, and the derivative on the left side is a material derivative. By expressing the background velocity and temperature with the subscript 0, the velocity and temperature can be written as

$$\boldsymbol{u} = \boldsymbol{U}_0 + \boldsymbol{V}, \quad T = T_0 + \theta, \quad (3)$$

where $\boldsymbol{V}$ is the velocity perturbation and θ is the temperature perturbation.

The background velocity is set to be a super-rotating flow with a velocity difference $\Delta\boldsymbol{U}_0$ between the outer boundary and the inner boundary, and it satisfies

$$\nabla^2\boldsymbol{U}_0 = 0.$$

In addition, the background temperature is set to be radially dependent and satisfies

$$\nabla^2 T_0 = 0,$$

with a higher temperature at the outer boundary and a lower temperature at the inner boundary.

By employing the Boussinesq approximation, the momentum equation can be written as

$$\frac{\partial\boldsymbol{V}}{\partial t} + \boldsymbol{U}_0\cdot\nabla\boldsymbol{V} + \boldsymbol{V}\cdot\nabla\boldsymbol{U}_0 + \boldsymbol{V}\cdot\nabla\boldsymbol{V} = -\nabla\pi + \nu\nabla^2\boldsymbol{V} + 2\boldsymbol{V}\times\boldsymbol{k}\Omega - \alpha\theta\Omega^2\boldsymbol{r}, \quad (4)$$

where π is the modified pressure, ν is the kinematic viscosity, $\boldsymbol{k}$ is the unit vector of the angular velocity, and α is a thermal expansion coefficient. The heat transfer equation can be written as

$$\frac{\partial\theta}{\partial t} + \boldsymbol{U}_0\cdot\nabla\theta + \boldsymbol{V}\cdot\nabla T_0 + \boldsymbol{V}\cdot\nabla\theta = \kappa\nabla^2\theta. \quad (5)$$

In writing the dimensionless equations, we let

$$x \to xd, \quad t = \frac{td^2}{\kappa}, \quad \theta = \theta\Delta T_0, \quad (6)$$

where d is the gap of the annulus and ΔT_0 is the background temperature difference between the outer boundary and the inner boundary. The quantities on the left sides of Equation (6) have dimension, and the quantities on the right sides of Equation (6) are dimensionless.

The dimensionless momentum equation is then

$$\frac{1}{Pr}\left(\frac{\partial \boldsymbol{V}}{\partial t}+\boldsymbol{V}\cdot\nabla\boldsymbol{V}\right)+\frac{1}{Pr}\Delta\widetilde{U_0}\left(1+\frac{1}{\ln\eta}\ln\frac{r_0}{r}\right)\frac{1}{r}\frac{\partial \boldsymbol{V}}{\partial\varphi}-\frac{1}{Pr}\Delta\widetilde{U_0}\frac{V_r}{\ln\eta}\frac{1}{r}\widehat{\boldsymbol{e}_\varphi}$$
$$=-\nabla\pi'+\nabla^2\boldsymbol{V}+\frac{d^2}{\nu}2\boldsymbol{V}\times\boldsymbol{k}\Omega-Ra\theta\boldsymbol{r},\tag{7}$$

where π' is the further modified pressure, $\widehat{\boldsymbol{e}_\varphi}$ is the unit vector of the azimuthal direction, and $\Delta\widetilde{U_0}$ is the nondimensional speed difference,

$$\Delta\widetilde{U_0}=\frac{d}{\kappa}\Delta U_0.$$

The nondimensional parameters, the Prandtl number Pr and Rayleigh number Ra (Chandrasekhar, 1961), are defined as

$$Pr=\frac{\nu}{\kappa},\quad Ra=\frac{\alpha\Delta T_0\Omega^2d^4}{\nu\kappa}.$$

The dimensionless heat equation is

$$\frac{\partial\theta}{\partial t}+\Delta\widetilde{U_0}\left(1+\frac{1}{\ln\eta}\ln\frac{r_0}{r}\right)\frac{1}{r}\frac{\partial\theta}{\partial\varphi}-\frac{V_r}{\ln\eta}\frac{1}{r}+\boldsymbol{V}\cdot\nabla\theta=\nabla^2\theta.\tag{8}$$

Expressing the velocity in terms of the stream function,

$$\boldsymbol{V}=\frac{1}{r}\frac{\partial h}{\partial\varphi}\widehat{\boldsymbol{e}_r}-\frac{\partial h}{\partial r}\widehat{\boldsymbol{e}_\varphi},$$

where $\widehat{\boldsymbol{e}_r}$ is the unit vector of the radial direction, and applying the operator

$$\boldsymbol{k}\cdot\nabla\times$$

to Equation (7), we have the momentum equation

$$-Ra\frac{\partial\theta}{\partial\varphi}+\nabla^4h-\frac{1}{Pr}\frac{\partial\nabla^2h}{\partial t}=\frac{1}{Pr}\frac{1}{r}\left(\frac{\partial h}{\partial\varphi}\frac{\partial\nabla^2h}{\partial r}-\frac{\partial h}{\partial r}\frac{\partial\nabla^2h}{\partial\varphi}\right)$$
$$+\frac{1}{Pr}\Delta\widetilde{U_0}\left(1+\frac{1}{\ln\eta}\ln\frac{r_0}{r}\right)\left(\frac{1}{r^3}\frac{\partial h}{\partial\varphi}+\frac{1}{r}\frac{\partial^3h}{\partial r^2\partial\varphi}+\frac{1}{r^3}\frac{\partial^3h}{\partial\varphi^3}\right)\tag{9}$$

and the heat transfer equation

$$\nabla^2\theta+\frac{1}{r^2}\frac{\partial h}{\partial\varphi}\frac{1}{\ln\eta}-\frac{\partial\theta}{\partial t}=\frac{1}{r}\frac{\partial h}{\partial\varphi}\frac{\partial\theta}{\partial r}-\frac{1}{r}\frac{\partial h}{\partial r}\frac{\partial\theta}{\partial\varphi}-\Delta\widetilde{U_0}\left(1+\frac{1}{\ln\eta}\ln\frac{r_0}{r}\right)\frac{1}{r}\frac{\partial\theta}{\partial\varphi}.\tag{10}$$

The boundary condition is set to

$$h=0,\quad\frac{\partial h}{\partial r}=0,\quad\theta=0.$$

For this study, the choice of parameters is set as follows: the Prandtl number $Pr=10.0$, the kinematic viscosity $\nu=1\times10^6\ \mathrm{m}^2\ \mathrm{s}$, the thermal diffusivity $\kappa=1\times10^5\ \mathrm{m}^2\ \mathrm{s}$, and the thermal expansion coefficient $\alpha=2\times10^{-4}\ \mathrm{K}^{-1}$ (Afanasyev and Huang YC, 2020). In addition, $\Delta\widetilde{U_0}$ is around tens to match the observation (Chaisson and McMillan, 1997). From here on, the solution is searched in nondimensional space.

The Rayleigh number Ra is the dominant parameter that controls the Rayleigh–Taylor instability. From a mathematical point of view, the terms of Equation (7) can be divided into three categories. The first one is the time rate of flow variation. The second one is the divergence of flux. The third one is the source. There are two source terms in Equation (7). One source term is the Coriolis force, which changes only the direction of the flow. (This point can be seen more clearly in Equation (9). There is no term related to the Coriolis force after applying the operator $\boldsymbol{k}\cdot\nabla\times$ to Equation (7)). Another source term related to the Rayleigh number is the buoyancy force, which changes the strength of the flow. It is this source that controls the Rayleigh–Taylor instability mathematically.

Physically, the constituents of the Rayleigh number indicate what factors play a role in the Rayleigh–Taylor instability. The quantities in the numerator of the Rayleigh number would excite the instability, whereas those in the denominator would suppress the instability. For example, Ω^2d has the role of centrifugal force (similar to gravity), which is a necessary factor related to the Rayleigh–Taylor instability. In addition, ΔT_0 is related to the heat entering or leaving the calculated domain through the outer and inner boundaries by conduction; it is the energy source for the instability. The α is related to the buoyancy force, an ingredient for convection, whereas ν, the viscosity, always inhibits the motion of flow. And κ, the thermal diffusivity, is related to thermal conduction, which is a competitive process of convection in heat transfer from the outer boundary to the inner boundary. All these quantities are combined together in a single parameter, the Rayleigh number. The mathematical power for each quantity is determined to make the Rayleigh number dimensionless.

3. Results

The super-rotation (represented by the velocity difference $\Delta\widetilde{U_0}$ between the outer boundary and the inner boundary) and the poleward heat transfer (represented by the Rayleigh number R) have opposite effects on the Rayleigh–Taylor instability. The poleward heat transfer stimulates the instability, whereas the super-rotation inhibits the instability. In a steady state, the mode number increases as the Rayleigh number increases, and it decreases as the velocity difference increases.

Without super-rotation (i.e., $\Delta\widetilde{U_0}=0$), the onset mode of instability is determined by η (the ratio of the radius of the inner boundary to the outer boundary), and it is an increasing function of η. For example, when η is 0.3, the onset mode is 3 (with the critical Rayleigh number $Ra=2.03\times10^3$); when η is 0.4, the onset mode is 4 (with the critical Rayleigh number $Ra=1.56\times10^3$); and when η is 0.5, the onset mode is 5 (with the critical Rayleigh number $Ra=1.38\times10^3$).

For this annulus domain of simulation, the finite difference is used in the radial direction, and the spectrum method is employed in the azimuthal direction. Figure 3 shows the growth process of Mode 5 for the case $\eta=0.5$, $Ra=1,750.0$, and $\Delta\widetilde{U_0}=6.0$. The last two panels show that the flow has reached a steady state.

Figure 4 shows the flow and temperature contours for $\eta=0.5$, $Ra=1{,}750.0$, and $\Delta\widetilde{U_0}=6.0$. The flow pattern demonstrates five cyclones. The Nusselt number, which is a measurement of the convective heat transport through the annulus, is shown in Figure 5 as a function of time. The constant value of the Nusselt number indicates that the flow is in a steady state. Figure 6 shows the flow and temperature contours for $\eta=0.5$, $Ra=1{,}750.0$, and

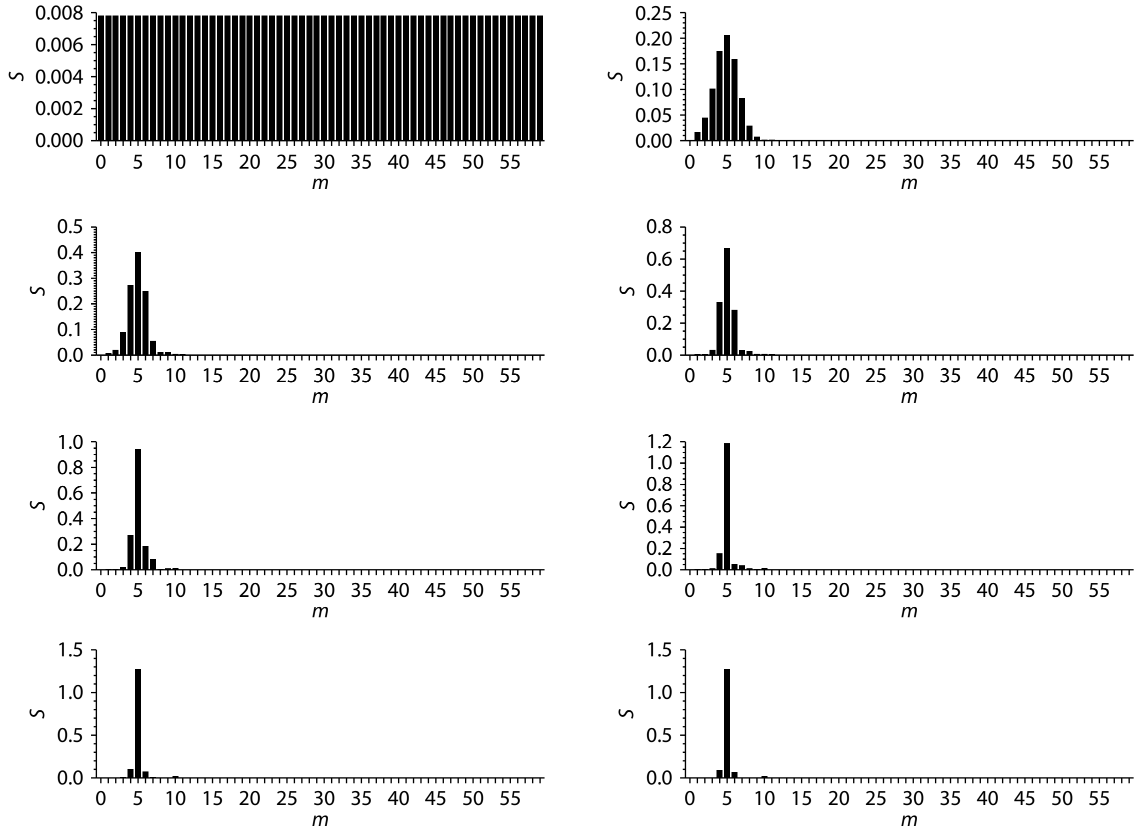

Figure 3. Spectrum bars showing the process of instability development for the case of η = 0.5, Ra = 1,750.0, and $\Delta\widetilde{U}_0$ = 6.0. The panels show the amplitude S of each mode m. The panels from top to bottom indicate the growth of Mode 5 as a function of time. The separation of dimensionless time between panels is 0.1.

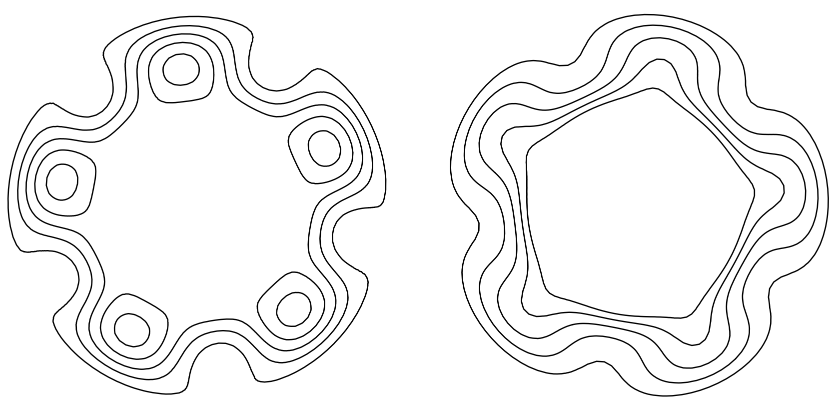

Figure 4. The contours of stream function (left panel) and temperature (right panel), where η = 0.5, Ra = 1,750.0, and $\Delta\widetilde{U}_0$ = 6.0. The patterns of flow and temperature are both in a steady state.

$\Delta\widetilde{U}_0$ = 5.0. The flow pattern demonstrates five cyclones (solid lines), with five tiny anticyclones (dashed lines) accompanying each of them. The Nusselt number of this case is so close to the case of $\Delta\widetilde{U}_0$ = 6.0 that the plot is not presented. These two flow patterns are consistent with the appearance of cyclones and anticyclones in the images taken by JIRAM (Adriani et al., 2018; Grassi et al., 2018).

The Mode 5 may also appear at lower η values. Figure 7 shows the flow and temperature contours for η = 0.4, Ra = 10,000.0, and $\Delta\widetilde{U}_0$ = 17.0. The flow pattern demonstrates five cyclones. The Nusselt number is plotted in Figure 5. Figure 8 shows the flow and temperature contours for η = 0.4, Ra = 10,000.0, and $\Delta\widetilde{U}_0$ = 16.0. The flow pattern demonstrates five cyclones, with five tiny anticyclones accompanying each of them. Figures 4 and 7 infer that Mode 5 may appear in the η range between 0.4 and 0.5.

Figure 9 shows the flow and temperature contours for η = 0.6, Ra = 10,000.0, and $\Delta\widetilde{U}_0$ = 30.0. The flow pattern demonstrates eight cyclones. The Nusselt number is plotted in Figure 5. Figure 10 shows the flow and temperature contours for η = 0.6, Ra = 10,000.0, and $\Delta\widetilde{U}_0$ = 23.0. The flow pattern demonstrates

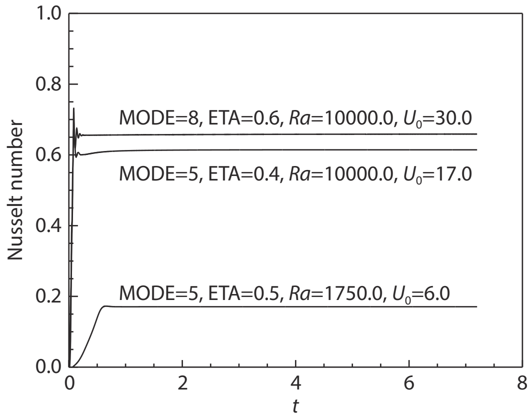

Figure 5. The Nusselt number as a function of time, the *t* is the dimensionless time.

eight cyclones, with eight tiny anticyclones accompanying each of them. These flow patterns are also consistent with prior observations (Adriani et al., 2018; Grassi et al., 2018).

A case without the inverse temperature gradient was also run (η = 0.5, Ra = 0.0, and $\Delta\widetilde{U}_0$ = 6.0). The amplitude of each mode decreased by more than one order of magnitude after time 0.006 (Figure 11). The decay of modes shows clearly that instability cannot be excited when the Rayleigh number is set to zero. In the final steady flow, only super-rotation is left. Such a flow pattern is similar to those in the polar regions of Saturn.

4. Discussion and Conclusions

The spin of Jupiter imposes a very strong mechanical constraint on its dynamics. The direction of the spin axis breaks the spherical symmetry that originates from the planetary self-gravity field. The centrifugal force sets up a potential analogue to gravity. Heavy elements move (sink) to the region farther out from the spin axis, and light elements move (rise) to the region near the spin axis. Similar to the case for gravity, a pressure gradient is built up by the centrifugal force. On Jupiter, a negative latitudinal pressure gradient exists because of the spin of the planet. In a stable situation, the pressure difference between the outer side of an element and the inner side balances the centrifugal force on it. However, when there is a negative temperature gradient along the latitude, the heavy element farther out is heated. It then expands, resulting in a lower density. The centrifugal force on the expanded element cannot balance the pressure difference. The buoyancy force brings the heated element to the near region close to the spin axis. In such a situation, the Rayleigh–Taylor instability takes place.

Unlike previous studies on cyclones in Jupiter's polar regions, which focused on the possible relation with the polar cyclones on

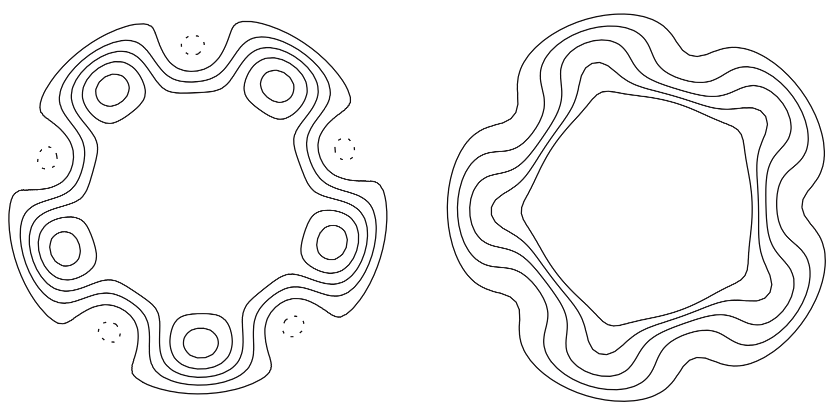

Figure 6. The contours of stream function (left panel) and temperature (right panel), where η = 0.5, Ra = 1,750.0, and $\Delta\widetilde{U}_0$ = 5.0. In the left panel, the solid lines indicate cyclones and the dashed lines indicate anticyclones. The patterns of flow and temperature are both in a steady state.

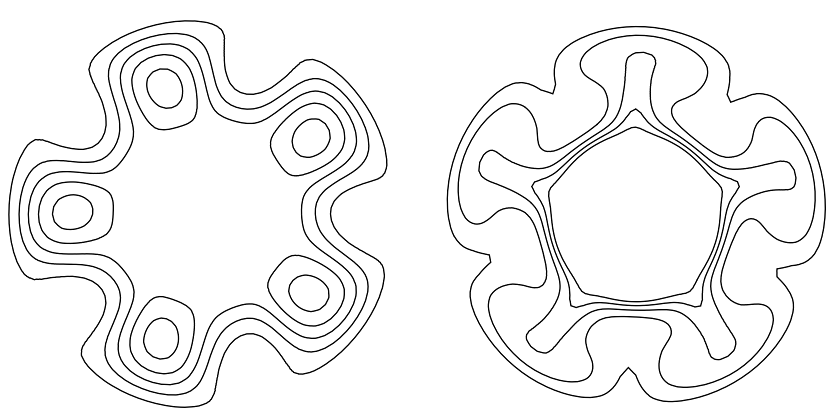

Figure 7. The contours of stream function (left panel) and temperature (right panel), where η = 0.4, Ra = 10,000.0, and $\Delta\widetilde{U}_0$ = 17.0. The patterns of flow and temperature are both in a steady state.

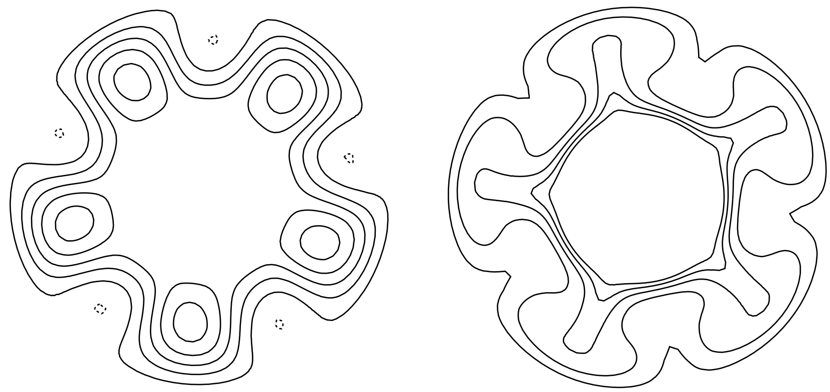

Figure 8. The contours of stream function (left panel) and temperature (right panel), where η = 0.4, Ra = 10,000.0, and $\Delta\widetilde{U}_0$ = 16.0. In the left panel, the solid lines indicate cyclones, and the dashed lines indicate anticyclones. The patterns of flow and temperature are both in a steady state.

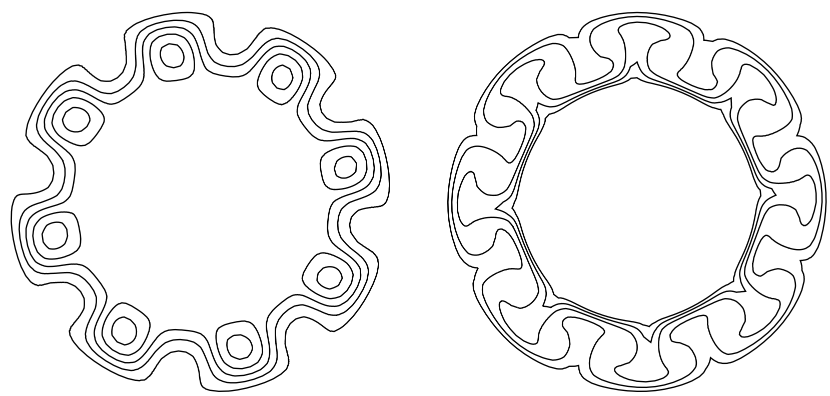

Figure 9. The contours of stream function (left panel) and temperature (right panel), where η = 0.6, Ra = 10,000.0, and $\Delta\widetilde{U}_0$ = 30.0. The patterns of flow and temperature are both in a steady state.

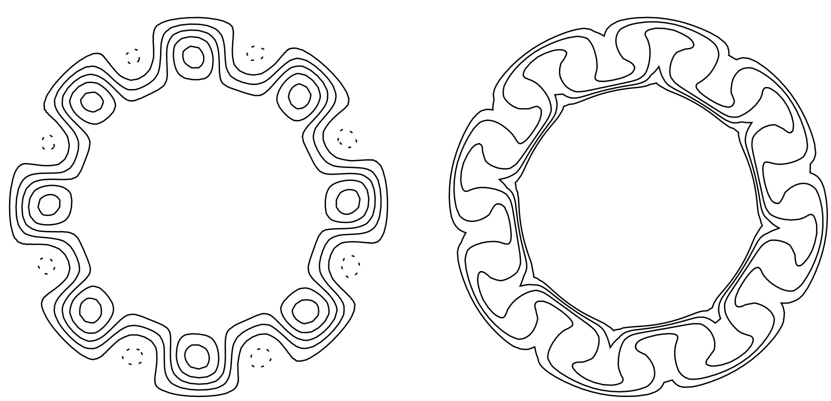

Figure 10. The contours of stream function (left panel) and temperature (right panel), where η = 0.6, Ra = 10,000.0, and $\Delta\widetilde{U}_0$ = 23.0. In the left panel, the solid lines indicate cyclones, and the dashed lines indicate anticyclones. The patterns of flow and temperature are both in a steady state.

Saturn (because of the similarity of the two planets as a whole), our investigation is inspired by the clustering of cyclones around the South Pole of the Earth. We think that the cyclones on Jupiter and the cyclones on the Earth are more closely related, as they may share the same physical mechanism. Figures 4 and 9 support this opinion.

The cyclones around the South Pole of the Earth are probably affected by three factors. The first is the western wind zone southward of the equator, the second is the negative temperature gradient with respect to the latitude, and the third is the centrifugal force resulting from the rotation of the Earth. The same factors may also exist in Jupiter's polar regions. The western wind zone and the centrifugal force are out of question. The negative temperature gradient may be related to solar radiation because of the small axial inclination of Jupiter.

For the problem we are interested in, the fundamental difference

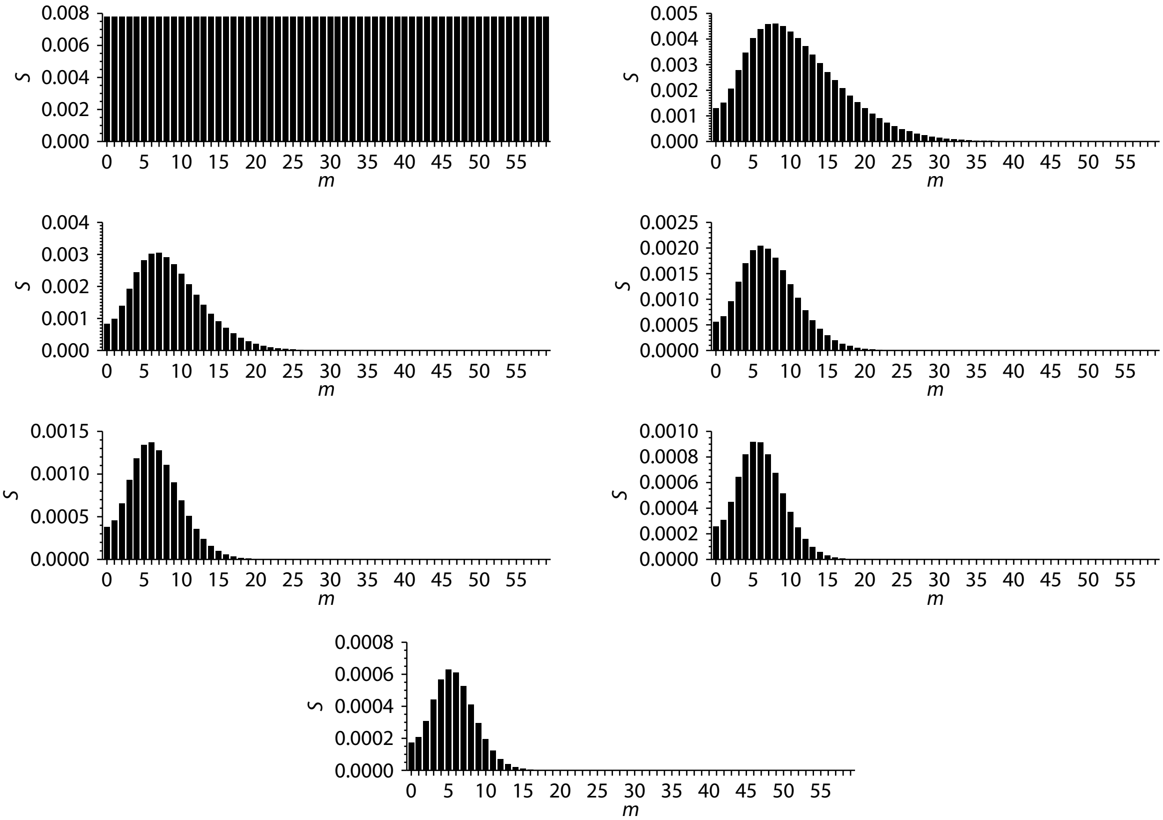

Figure 11. Spectrum bars showing the process of instability development for the case of η = 0.5, Ra = 0.0, and $\Delta\widetilde{U}_0$ = 6.0. The panels show the amplitude of each mode. The panels from top to bottom indicate the decay of modes as a function of time. The separation of dimensionless time between panels is 0.001.

between Jupiter and Saturn is the axial inclination. For Jupiter, the axial inclination is about 3.12°, whereas for Saturn, the axial inclination is approximately 26.73° (http://www.krysstal.com/solarsys_planets.html). The very small axial inclination of Jupiter guarantees a negative temperature gradient, which is symmetric around each pole. For Saturn, because of the large axial inclination, the appearance of a negative temperature gradient may be very difficult. Here, we wish to point out that although the axial inclination of the Earth is approximately 23.5°, the symmetry of the temperature gradient about its South Pole is maintained by the icy continent Antarctica.

The great difference between our investigation and the previous studies is the negative temperature gradient with respect to latitude. Combined with the centrifugal force, a radially orientated Rayleigh–Taylor instability takes place. It is this Rayleigh–Taylor instability that modulates or controls the patterns of flow in the polar regions. The mode of cyclones may be controlled by the annular gap where the latitudinal temperature gradient appears. A larger gap yields a relative smaller mode, as illustrated by Figure 4 for Mode 5, whereas a smaller gap results in a larger mode, as illustrated by Figure 9 for Mode 8.

If our interpretation about the occurrence of clustering cyclones is correct, seasonal variation is possible, meaning the number of cyclones at each pole would change with the seasons. For example, the number of cyclones at the northern pole would change from eight to five in the period of Jupiter's rotation around the Sun.

From the critical Rayleigh number value, a very small temperature difference between the outer boundary and the inner boundary can be inferred. This small temperature difference is easily induced by solar radiation.

Figure 5 may provide the answer for the persistence of the flow pattern, namely, that the flow is in a steady state. Here, a unit of nondimensional time corresponds to 2.5×10^8 s, or eight Earth years.

It is noteworthy that super-rotation has the lowest centrifugal potential among all the types of motion (e.g., sub-rotation). Thus, it is a reasonable choice for the background velocity.

In conclusion, our simulations strongly suggest that the cyclones in the polar regions of Jupiter are modulated or controlled by the radially directional Rayleigh–Taylor instability driven by centrifugal force and the negative temperature gradient along the latitude.

Acknowledgments

This work was supported by the National Nature Science Foundation of China (Grant No. NSFC41974204).

References

Adriani, A., Filacchione, G., Di Iorio, T., Turrini, D., Noschese, R., Cicchetti, A., Grassi, D., Mura, A., Sindoni, G., … Olivieri, A. (2017). JIRAM, the Jovian Infrared Auroral Mapper. *Space Sci. Rev.*, *213*(1), 393–446. https://doi.org/

10.1007/s11214-014-0094-y

Adriani, A., Mura, A., Orton, G., Hansen, C., Altieri, F., Moriconi, M. L., Rogers, J., Eichstädt, G., Momary, T., … Amoroso, M. (2018). Clusters of cyclones encircling Jupiter's poles. *Nature*, *555*(7695), 216–219. https://doi.org/10.1038/nature25491

Afanasyev, Y. D., and Huang, Y. C. (2020). Poleward translation of vortices due to deep thermal convection on a rotating planet. *Geophys. Astrophys. Fluid Dyn.*, *114*(6), 821–834. https://doi.org/10.1080/03091929.2019.1694676

Bolton, S. J., Adriani, A., Adumitroaie, V., Allison, M., Anderson, J., Atreya, S., Bloxham, J., Brown, S., Connerney, J. E. P., … Wilson, R. (2017). Jupiter's interior and deep atmosphere: The initial pole-to-pole passes with the Juno spacecraft. *Science*, *356*(6340), 821–825. https://doi.org/10.1126/science.aal2108

Chaisson, E., and McMillan, S. (1997). *Astronomy Today* (2nd ed). New York: Prentice Hall.

Chandrasekhar, S. (1961). *Hydrodynamic and Hydromagnetic Stability*. Oxford: Clarendon Press.

Chen, C. X., and Zhang, K. K. (2002). Nonlinear convection in a rotating annulus with a finite gap. *Geophys. Astrophys. Fluid Dyn.*, *96*(6), 499–518. https://doi.org/10.1080/0309192021000071320

Connerney, J. E. P., Adriani, A., Allegrini, F., Bagenal, F., Bolton, S. J., Bonfond, B., Cowley, S. W. H., Gerard, J. C., Gladstone, G. R., … Waite, J. (2017). Jupiter's magnetosphere and aurorae observed by the Juno spacecraft during its first polar orbits. *Science*, *356*(6340), 826–832. https://doi.org/10.1126/science.aam5928

Grassi, D., Adriani, A., Moriconi, M. L., Mura, A., Tabataba-Vakili, F., Ingersoll, A., Orton, G., Hansen, C., Altieri, F., … Amoroso, M. (2018). First estimate of wind fields in the Jupiter polar regions from JIRAM-Juno images. *J. Geophys. Res.: Planets*, *123*(6), 1511–1524. https://doi.org/10.1029/2018JE00555

Hansen, C. J., Caplinger, M. A., Ingersoll, A., Ravine, M. A., Jensen, E., Bolton, S., and Orton, G. (2014). Junocam: Juno's outreach camera. *Space Sci. Rev.*, *213*(1), 475–506. https://doi.org/10.1007/s11214-014-0079-x

O'Neill, M. E., Emanuel, K. A., and Flierl, G. R. (2015). Polar vortex formation in giant-planet atmospheres due to moist convection. *Nat. Geosci.*, *8*(7), 523–526. https://doi.org/10.1038/ngeo2459

Reinaud, J. N., and Dritschel, D. G. (2019). The stability and nonlinear evolution of quasi-geostrophic toroidal vortices. *J. Fluid Mech.*, *863*, 60–78. https://doi.org/10.1017/jfm.2018.1013

Rhines, P. B. (1975). Waves and turbulence on a beta-plane. *J. Fluid Mech.*, *69*(3), 417–443. https://doi.org/10.1017/S0022112075001504

Shapiro, L. J. (1992). Hurricane vortex motion and evolution in a three-layer model. *J. Atmos. Sci.*, *49*(2), 140–154. https://doi.org/10.1175/1520-0469(1992)049<0140:HVMAEI>2.0.CO;2

Theiss, J. (2006). A generalized Rhines effect and storms on Jupiter. *Geophys. Res. Lett.*, *33*(8), L08809. https://doi.org/10.1029/2005GL025379

Zhang, K. K., Chen, C. X., and Greed, G. T. (1999). Finite-amplitude convection rolls with integer wavenumbers. *Geophys. Astrophys. Fluid Dyn.*, *90*(3-4), 265–296. https://doi.org/10.1080/03091929908204122